https://doi.org/10.1016/j.jpowsour.2018.10.013

AgSn intermetallics as highly selective and active oxygen reduction electrocatalysts in membraneless alkaline fuel cells

Qiao Wang,[a] Fuyi Chen, [a, *] Yaxing Liu,[a] Tesfaye Tadesse Gebremariam,[a] Junpeng Wang,[a] Liang An[b] and Roy L. Johnston[c]

[a]State Key Laboratory of Solidication Processing, Northwestern Polytechnical University, Xi'an, 710072, China

[b]Department of Mechanical Engineering, The Hong Kong Polytechnic University, Hung Hom, Kowloon, Hong Kong Special Administrative Region, China

[c]School of Chemistry, University of Birmingham, Birmingham, B15 2TT, U.K

[*]**Corresponding author:**

[*]Fuyi Chen

[a]127 West Youyi Road Xi'an Shaanxi, 710072 P. R. China.

E-mail address: fuyichen@nwpu.edu.cn

Abstract: The Ag_4Sn and Ag_3Sn intermetallics are successfully synthesized by combining electrochemical deposition and dealloying methods. The Ag_4Sn and Ag_3Sn possess a half-wave potential of 0.810 mV and 0.790 mV respectively for the oxygen reduction reaction in alkaline media, which are comparable to the commercial Pt/C (0.837 mV). In term of the durability, the Ag_4Sn retains a half-wave potential of 0.775 mV after 5000 potential cycles, which is superior to Pt/C of 0.784 mV. The better catalytic activity and durability are mainly attributed to the ensemble effect and strong chemical bond in the AgSn ordered intermetallic structure. The catalytic activity is hardly influenced by methanol or ethanol in alkaline media with alcohol concentrations up to 1.0 M. Therefore, a membraneless alkaline zinc-air battery and direct alcohol fuel cell can operate with Ag_4Sn and Ag_3Sn intermetallics as the cathode catalysts, which allow the anode fuel to freely enter the cathode. A high power density is delivered by the membraneless alkaline fuel cells with zinc, methanol or ethanol as anode fuels. The excellent alcohol-tolerance is beneficial to the oxygen reduction reaction of alkaline fuel cells and makes the AgSn intermetallics a promising candidate to replace Pt-based electrocatalysts for oxygen reduction reaction.

Keywords: Oxygen reduction reaction; Intermetallic; Silver; Tin; Membraneless alkaline fuel cells

1. Introduction

The alkaline fuel cells have been developed to meet rapidly rising energy demand and to resolve environmental issues owing to their fascinating features, including large energy density, high energy efficiency, easy storage/transportation, and low/zero emission [1-5]. In comparison to the acid fuel cells, they also offer the facile kinetics of electrode reaction and avoid the corrosive problems of catalysts, especially using the transition metals (e.g. Fe, Co, Ni, Cu) [6]. For the alkaline fuel cells, an anion-exchange membrane is necessary to separate the anode and the cathode while providing OH^- migration [7]. More importantly, this membrane can prevent the crossover of fuel and oxidant between the anode and cathode to maximize the power output of the fuel cell [8]. However, the state-of-the-art anion-exchange membranes still suffer from the poor ionic conductivity, the limited stability, the high rate of alcohol crossover and the lack of industrial production [9,10]. On the other hand, the use of the membrane severely restricts the device design, limits the electrolyte choice and increases the cell cost. Therefore, a membraneless alkaline fuel cell that avoids the above obstacles has recently attracted much attention.

As far as we are aware, the membraneless alkaline fuel cells can be divided into two types: laminar flow-based fuel cells and fuel cells with alcohol-tolerant cathode catalysts. Laminar flow-based fuel cells are difficult to be scaled up for a single cell due to the millimeter-scale size [11]. Even through improving cell designs, stacking or multiplexing technology, this type of membraneless fuel cells are not yet satisfactory for the practical applications in terms of power and cost [12-14]. Hence, the membraneless alkaline fuel cells mainly based on alcohol-tolerant cathode catalysts are of particularly interest, which

achieve more flexibility and miniaturizability in cell design, simpler implementation, and low cost. Central to the operation of all the membraneless alkaline fuel cells is the efficient, alcohol-tolerant oxygen reduction reaction (ORR) catalyst. In spite of the prohibitive cost and low reserves [15], in addition to the sluggish kinetics and poor durability [16,17], platinum (Pt) is the most popular electrocatalyst for the ORR in alkaline fuel cells, but their ORR performances are easily degraded due to the mixed-potential and catalyst poisoning forming at the cathode. This is because Pt catalyst is also catalytically active toward alcohols so that the serious alcohol crossover through the membrane leads to the significant decay of the cell performance [18-20].

Considerable efforts and progresses have been made to develop the alcohol-tolerant Pt-based ORR catalysts [21-28]. For instance, Guo and co-workers [22] reported a PtBi intermetallic nanocatalyst, which offers an excellent methanol tolerance but a lower ORR activity than that of the commercial Pt/C catalyst. Jeyakumar group [23] developed the $Au_{85}Pt_{15}$/C catalyst, which showed both excellent methanol tolerance behavior and better ORR performance in terms of the mass activity and power density in a single fuel cell as compared to that using the commercial Pt/C catalyst. Cho et al. [24] prepared the PtPdCo/C ternary electrocatalysts, which exhibited a similar ORR activity and superior methanol tolerance as compared to Pt/C. The PtPd nanoflowers [25], PtNi intermetallics [26], Pt nanoparticles on $CoSe_2$ nanobelts [27], and Pt nanoparticles encapsulated in nitrogen-doped carbon nanocages [28] were found to be insensitive to methanol so that they display an improved methanol tolerance performance and can be used for alcohol-tolerant ORR catalysts.

However, such Pt-based ORR electrocatalysts still show relatively low methanol

tolerance due to the limited suppression of alcohol oxidation reaction (AOR). To address this issue, recent research has been focused on Ag-based alcohol-tolerant catalysts, which have a much lower cost than Pt-based catalysts. As compared with Pt-based catalysts, the Ag-based catalysts possess a similar ORR mechanism and kinetics but a higher tolerance to alcohol [29-31]. Currently, Ag and Ag-based alloys exhibit good alcohol-tolerant capability while maintain high ORR activity. For instance, Zeng and Ni et al. [32,33] reported the Ag nanowires exhibited a good activity and alcohol-tolerant stability for the ORR in alkaline media. Lu et al. [34] reported that Ag_4Sn intermetallic nanoparticles displayed better ORR performance and excellent tolerance to methanol, but no durability test was investigated. In our previous work, we have found that the Ag_3Sn nano-intermetallic can be used as a good bifunctional electrocatalyst for ORR and borohydride oxidation reaction (BOR) [35]. Taylor et al. [31] synthesized a silver palladium core-shell catalyst on multiwall carbon nanotubes by galvanic displacement of Pd on Ag nanoparticles, the Ag@Pd catalysts showed a high ORR activity and alcohol-tolerant capability in the presence of methanol and ethanol. In the presence of methanol, the current density on Ag@Pd decreased by 0.18 mA/cm^2, compared to Pt/C (0.97 mA/cm^2) and Pd/C (1.09 mA/cm^2). Unfortunately, the state-of-the-art Ag-based alcohol-tolerant catalysts demonstrate a lower ORR activity and inferior long-term stability in comparison to Pt-based catalysts.

In this work, we develop the novel AgSn intermetallic catalysts with different compositions and morphologies, synthesized via combining electrochemical deposition and dealloying methods. The precursor alloys with various surface morphology and elemental compositions are prepared by tuning the deposition current, afterwards, the

pure phase Ag_4Sn and Ag_3Sn intermetallic catalysts are obtained by dealloying in diluted $HClO_4$. The Ag_4Sn and Ag_3Sn catalysts possess a half-wave potential of 0.810 mV and 0.790 mV for the ORR activity, which is comparable to the commercial Pt/C catalyst. The Ag_4Sn exhibits superior stability with only 35 mV shift in $E_{1/2}$ after 5000 potential cycles. More importantly, this AgSn intermetallic with relatively high ORR activity is insensitive to alcohol crossover into the cathode and performs well at high alcohol concentration, which makes it promising to exclude the alkaline anion-exchange membrane from the cell. Building on the promising selective ORR activity in the presence of the alcohol, three membraneless alkaline fuel cells are demonstrated with zinc, methanol, and ethanol as anode fuels.

2. Experimental

2.1. Preparation of samples

2.1.1 Electrodeposition of precursor alloy

The Ag_xSn_{100-x} alloy was synthesized using a three-electrode system containing a glassy carbon working electrode, platinum sheet counter electrode and saturated calomel electrode (SCE) reference electrode. The electroplating solution was composed of 2.0 M H_2SO_4, 0.2 M $SC(NH_2)_2$, 0.025 M $SnSO_4$, and 0.01 M Ag_2SO_4. Electrodeposition was carried out galvanostatically with mild agitation until the quantity of electricity approached to 0.3 mC cm^{-2}. The $Ag_{75}Sn_{25}$ and $Ag_{50}Sn_{50}$ precursor alloys were deposited at a current density of 10.2 and 25.5 mA cm^{-2}, respectively, whose atomic ratios of Ag/Sn were measured by the energy-dispersive X-ray spectrometer of scanning electron microscopy. The as-synthesized alloys were washed with DI water, and then dried in nitrogen at room temperature.

2.1.2 Dealloying of precursor alloy

To remove Sn and adjust the Ag/Sn ratio, the electrochemical dealloying was conducted within a potential range of -0.45 V to 0 V in a N_2-purged 0.1 M $HClO_4$ solution at a scan rate of 50 mV s^{-1} for several cycles.

2.2. Physical characterization

The morphology, structure, and composition of the samples were characterized by a field-emission scanning electron microscopy (FESEM, FEI NovaSEM 450) with an energy-dispersive X-ray spectrometer (EDX) detector, and high-resolution transmission electron microscopy (HRTEM, FEI Tecnai F30), X-ray diffraction (XRD) (PANalytical X'Pert Pro MPD, Cu Kα radiation of 1.5406 Å), and X-ray photoelectron spectroscopy (XPS) (ESCALAB 250).

2.3. Electrochemical characterization

Electrochemical investigations were carried out at room temperature using CHI 660C electrochemical workstation (Chenhua, China). The working electrode was prepared by electrodepositing the catalyst on the glassy carbon rotating disk electrode (GC-RDE, 5 mm in diameter). Pt wire and Hg/HgO electrode were used as the counter and reference electrodes, respectively. All potentials in this paper were reported relative to the reversible hydrogen electrode (RHE) unless indicated. The ORR activities of the catalysts were examined in 0.1 M KOH solution saturated with oxygen. Linear scanning voltammetry (LSV) curves at different rotation rates were performed with a scan rate of 10 mV s^{-1}. The alcohol tolerances (methanol and ethanol) were examined by adding alcohols at different concentrations (ranging from 1 mM to 1 M) to the alkaline electrolyte saturated with oxygen. The ORR response in the presence of alcohols was

obtained at a scan rate of 10 mV s^{-1} and at a rotation speed of 1600 rpm. For comparison, the commercial Pt/C (Johnson Matthey, 20 wt. %) was also tested. The electrochemical surface area (ECSA) of Ag-based materials was measured using Pb-stripping voltammetry. Pb-stripping voltammetry was conducted by holding the potential at 0.20 V and then sweeping to 0.7 V at 10 mV s^{-1} in N_2-saturated 0.1 M KOH + 125 μM $Pb(NO_3)_2$ solution. ECSAs were calculated by integrating the charge associated with Pb underpotential deposition (UPD) on the catalysts and using a conversion factor of 280 uC cm^{-2}. For the commercial Pt/C catalyst, cyclic voltammetry (CV) was performed within the potential range of +0.07 V to +1.12 V at a scan rate of 50 mV s^{-1} in 0.1 M KOH with N_2 saturation. ECSAs were established by integrating the hydrogen desorption peak and using a conversion factor of 210 μC cm^{-2}.

2.4. The membraneless alkaline fuel cell performance testing

The membraneless alkaline zinc-air battery and direct alcohol fuel cell (DAFC) are assembled as a home designed cell configuration. The membraneless alkaline Zn-air battery was built with a zinc plate, the air electrode and 6 M KOH electrolyte. The membraneless alkaline DAFCs with 0.785 cm^2 active area were fabricated with Pt/C (1.5 mg cm^{-2}) anode and AgSn intermetallics cathode (0.3 mg cm^{-2}). The space between two electrodes was filled with an aqueous electrolyte with 2 M KOH and 5 M alcohol. The performance was tested on a battery testing station (Neware Company, Shenzhen). Each current applied was allowed to stabilize for 5 min.

3. Results and discussion

3.1. Catalytic activity of AgSn intermetallic catalysts towards the ORR

The catalytic activity of the Ag_4Sn and Ag_3Sn towards the ORR was studied by LSV, and

benchmarked against the commercial Pt/C catalyst. Fig. 1a displays ORR polarization curves of AgSn intermetallics and Pt/C reference catalysts obtained in O_2-saturated 0.1 M KOH solution at a rotation rate of 1600 rpm. The Pt/C exhibited a half-wave potential ($E_{1/2}$) of 0.837 V and a diffusion-limiting current of 5.286 mA cm^{-2}. The Ag_4Sn intermetallic showed an $E_{1/2}$ value of 0.810 V and the diffusion-limiting current of 5.29 mA cm^{-2}, indicating the ORR activity of Ag_4Sn is comparable to that of Pt/C. The Ag_3Sn showed negative shift in $E_{1/2}$ of 20 mV relative to Ag_4Sn. The $E_{1/2}$ for the PtRu/C was 0.73 V, suggesting the poor activity for ORR.

The ORR activity of these different catalysts was further compared in terms of the mass-transport corrected Tafel plots in Fig. 1b. The Tafel slope increased in the following order: Ag_4Sn (63.53 mV $decade^{-1}$) < Ag_3Sn (67.28 mV $decade^{-1}$) < Pt/C (70.58 mV $decade^{-1}$). The lower Tafel slopes than Pt/C catalyst suggest that Ag_4Sn and Ag_3Sn exhibit remarkable catalytic activity in alkaline media. Since specific activity relies on the active site area, the electrochemical active surface areas (ECSAs) of the catalysts were measured. As shown in Fig. 1c, on the basis of Pb stripping, the ECSAs of Ag_4Sn and Ag_3Sn were calculated to be 0.967 and 0.725 $m^2\ g^{-1}$, respectively. The ECSA of Pt/C was 56 $m^2\ g^{-1}$ by integrating the charge related to the hydrogen desorption (Fig. S1). Fig. 1d shows the specific activities of Pt/C, Ag_4Sn, and Ag_3Sn at 0.85V, whose specific activities are 0.268, 0.193, and 0.155 mA cm^{-2}, respectively, indicating that the Ag_4Sn catalyst approaches to the 72% activity of Pt/C at a cost of 2%.

To gain further insight into O_2 reduction kinetics, the LSV curves were recorded on these catalysts at different rotating speeds (Fig. S2). A higher rotating speed results in a larger diffusion-limiting current, due to more O_2 delivery to the electrode surface. To

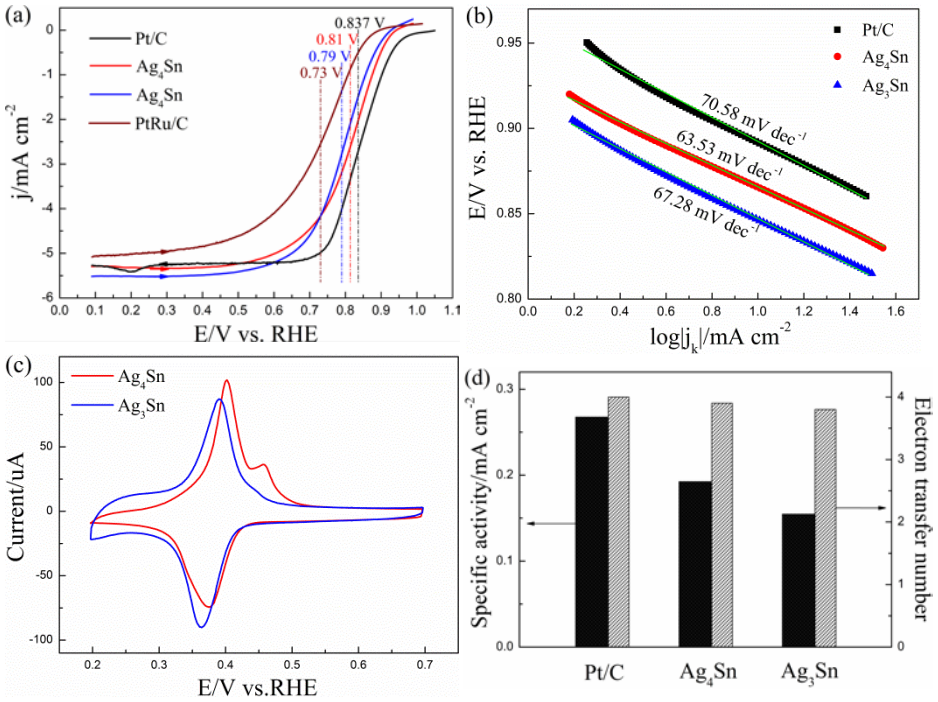

Fig. 1. (a) ORR polarization curves for the Ag_4Sn, Ag_3Sn, commercial Pt/C and PtRu/C catalysts recorded in O_2-saturated 0.1 M KOH solution at a rotation rate of 1600 rpm and a scan rate of 10 mV s^{-1}. (b) Mass-corrected Tafel plots of the Ag_4Sn, Ag_3Sn and commercial Pt/C catalysts. (c) Cyclic voltamograms of the Ag_4Sn and Ag_3Sn catalysts in N_2-purged 0.1 M KOH + 125 μM $Pb(NO_3)_2$ at a scan rate of 10 mV s^{-1}. (d) The specific activities at 0.85 V and the electron transfer numbers (n) for the Ag_4Sn, Ag_3Sn and commercial Pt/C catalysts.

calculate the electron transfer number for the ORR, the Levich plot derived from the Koutecky−Levich equation (K-L) [36] is shown in Fig. S2e.

$$j_{lim} = 0.62nFAD^{2/3}\nu^{-1/6}C_0\omega^{1/2} \quad (1)$$

where j_{lim} is the limiting current density, n is the number of electrons transferred, F is the Faraday constant (96485 C mol^{-1}), A is electrode area (0.196 cm^2), D is the diffusion coefficient of oxygen in 0.1 M KOH (1.9×10^{-5} cm^2 s^{-1}), ν is the kinematic viscosity (0.01

$cm^2\ s^{-1}$), C_0 is the oxygen concentration (1.2×10^{-3} mol L^{-1}) and ω is the electrode rotation speed (rad s^{-1}). The corresponding K-L plots at 0.3 V show good linearity, demonstrating first-order reaction kinetics with regard to dissolved O_2. In addition, based on the slopes of the K-L plots, the numbers of electron involved (n) for Ag_4Sn, Ag_3Sn, and Pt/C were established to be 3.9, 3.8, and 4.0, which implies that the Ag_4Sn catalysts can electrochemically reduce O_2 via a four-electron pathway, similar to the selectivity of Pt/C catalyst in oxygen reduction process.

3.2. Comparison of precursor alloy and dealloying derived catalysts

3.2.1. ORR activity

These high performance AgSn intermetallic catalysts were made from the Ag_xSn_{100-x} (e.g. $Ag_{75}Sn_{25}$ and $Ag_{50}Sn_{50}$) precursor alloy by selectively dealloying the less noble metal Sn. According to the electrochemical dealloying method shown in Fig. S3, the potential cycles between -0.45 V and +0 V were applied in order to remove Sn. Fig. 2(a,b) show that Sn was dissolved into the solution in the positive scan, as evidenced by the Sn oxidation peak between -0.2 V and 0 V, and Sn was re-deposited on the nanoparticles during the inverse scan, as indicated by the cathodic peak around at -0.22 V. With the cycling, the Sn redox peaks declined step by step in Fig. 2(a,b), however, the Pb-stripping peak current increased after 4 cycles for $Ag_{75}Sn_{25}$ and 15 cycles for $Ag_{50}Sn_{50}$ (insets of Fig. 2(c,d)), indicating that the specific surface of the precursor alloy is increased by the electrochemical dealloying, and the precursor alloy became Ag-rich when Sn atoms can be purposely dissolved. The ORR activity of dealloyed $Ag_{75}Sn_{25}$ and $Ag_{50}Sn_{50}$ alloys were monitored by the rotating disk electrode method, as observed in Fig. 2(c,d). The $E_{1/2}$ for $Ag_{75}Sn_{25}$ alloy had an initial value of 0.797 V in O_2-saturated 0.1 M KOH solution at

1600 rpm, positively shifted about 13 mV after dealloying for 4 cycles, but decreased after 8 cycles. Similarly, the $E_{1/2}$ value of the dealloyed $Ag_{50}Sn_{50}$ alloy positively shifted for the most 27 mV after 15 cycles. The reason for the activity enhancement is

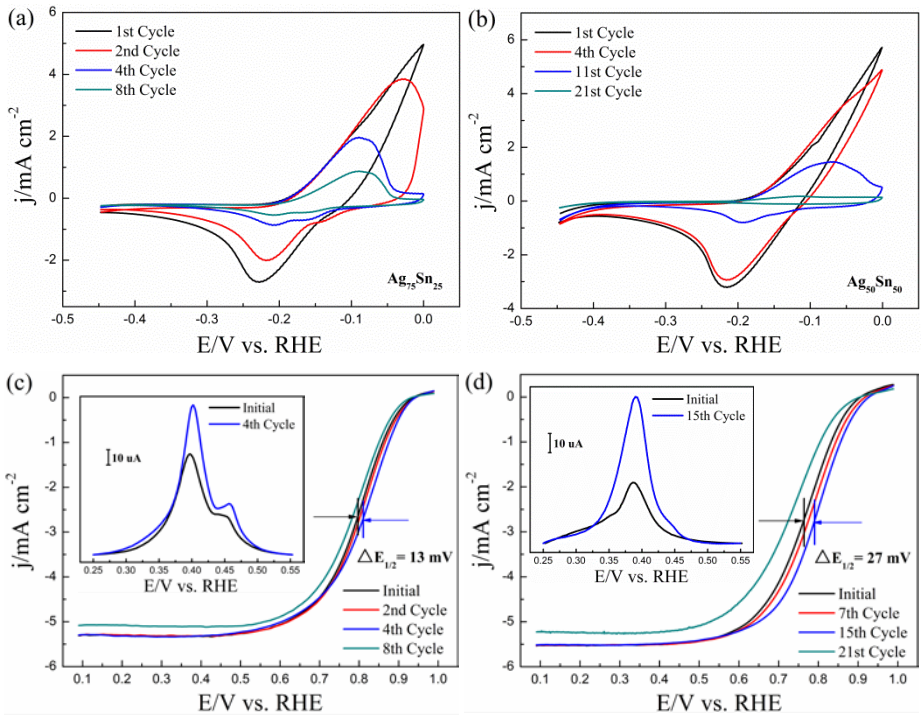

Fig. 2. (a, b) Cyclic voltamograms of $Ag_{75}Sn_{25}$ and $Ag_{50}Sn_{50}$ precursor alloy during the electrochemical dealloying in N_2-saturated 0.1 M $HClO_4$ at a scan rate of 50 mV s^{-1}. (c, d) ORR activity changed during dealloying of $Ag_{75}Sn_{25}$ and $Ag_{50}Sn_{50}$ precursor alloy as measured by polarization curves in O_2-saturated 0.1 M KOH at a rotation rate of 1600 rpm and a scan rate of 10 mV s^{-1}. Insets: ECSA before and after dealloying as measured by the Pb-stripping voltammograms.

assumingly contributed to the dealloying derived AgSn intermetallic catalyst, whose formation was further investigated as following.

3.2.2. Morphology and structure

As shown in Fig. 3(a,b), the morphology and Sn contents of precursor alloys can be easily tuned by simply varying the deposition current. When the deposition current density was 10.2 mA cm^{-2}, the as-prepared $Ag_{75}Sn_{25}$ precursor alloy consisted of plate-

like and little grainy structures and the molar ratio of Ag to Sn was determined to be 75:25 by SEM-EDX (Fig. S4). The as-prepared $Ag_{50}Sn_{50}$ precursor alloy nanoparticles with near-spherical shape were obtained at high current density of 25.5 mA cm^{-2}. After dealloying for 4 and 15 cycles, Ag_4Sn and Ag_3Sn intermetallics were made from the $Ag_{75}Sn_{25}$ and $Ag_{50}Sn_{50}$ precursor alloy, respectively. As shown in Fig. 3(c,d), the

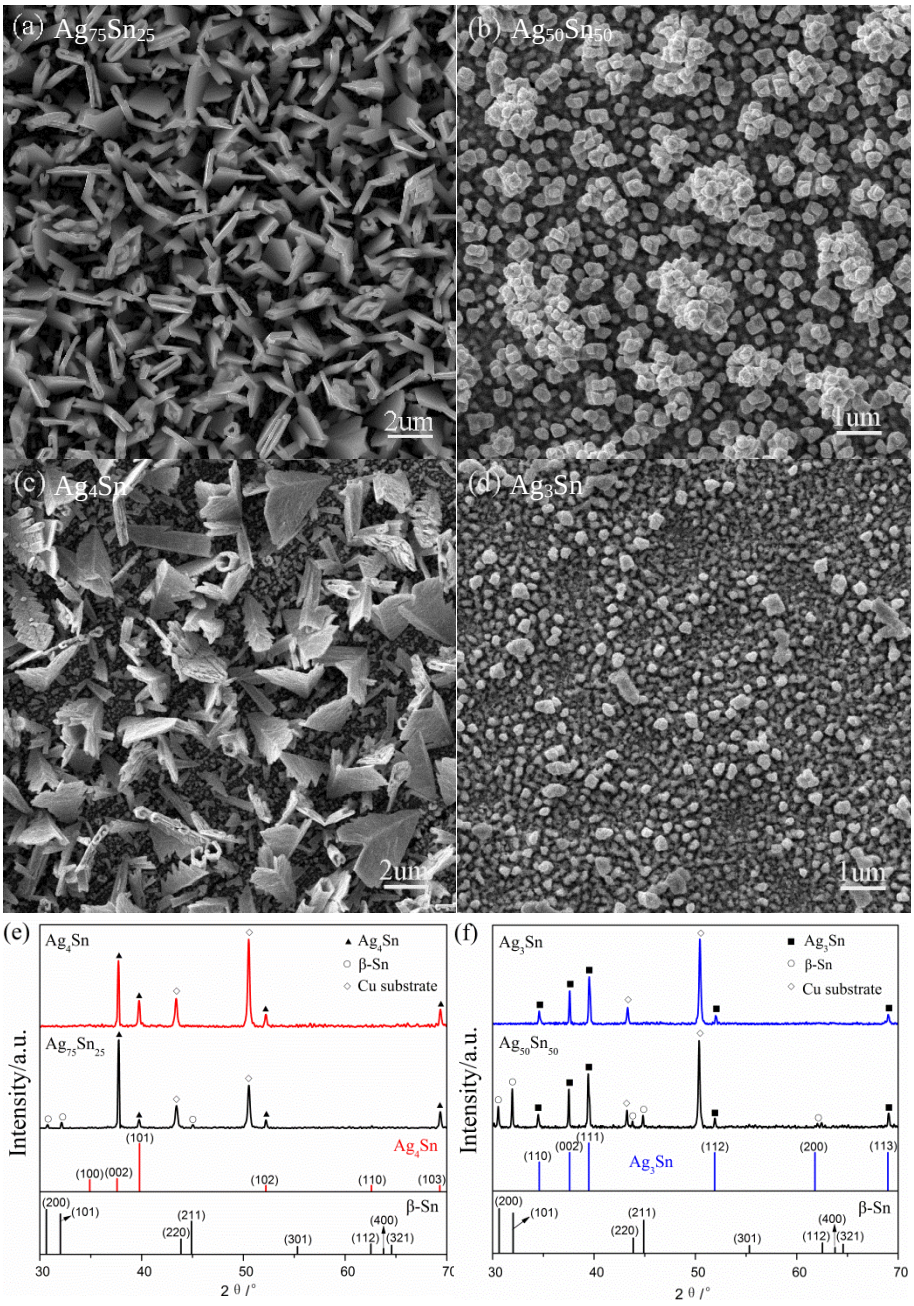

Fig. 3. (a, c) SEM images of $Ag_{75}Sn_{25}$ precursor alloy and dealloying derived Ag_4Sn catalysts. (b, d) SEM images of $Ag_{50}Sn_{50}$ precursor alloy and dealloying derived Ag_3Sn catalysts. (e) XRD patterns of $Ag_{75}Sn_{25}$ precursor alloy and dealloying derived Ag_4Sn catalysts. (f) XRD patterns of $Ag_{50}Sn_{50}$ precursor alloy and dealloying derived Ag_3Sn catalysts. The vertical lines represent the peak positions of the β-Sn (JCPDS No. 04-0673, black line), Ag_4Sn (JCPDS No. 29-1151, red line) and Ag_3Sn (JCPDS No. 04-0800, blue line) reflections, respectively.

presence of fish-like dendrites is observed in Ag_4Sn intermetallic and finer dispersed nanoparticles are evident for Ag_3Sn intermetallic. The dendrites or finer nanoparticles can help rapidly transfer charges and expose more catalytic active sites, further improving the ORR activity as observed in Fig. 2(c,d). The $Ag_{75}Sn_{25}$ precursor alloy was also dealloyed for 8 cycles, there is little change of the morphology and the Sn content decays to 18.86 (Fig. S5). The crystalline structure of the precursor alloy and dealloying derived AgSn intermetallic catalysts was confirmed using XRD, as shown in the diffraction patterns of Fig. 3(e,f), the tetragonal Ag_4Sn (# 29-1151) and β-Sn (# 04-0673) phases were formed for $Ag_{75}Sn_{25}$ precursor alloy, whose final product after dealloying for 4 cycles exhibited the same diffraction peaks to Ag_4Sn intermetallic. The $Ag_{50}Sn_{50}$ precursor alloy deposited at a high current density was a mixture of orthorhombic Ag_3Sn phase (# 04-0800) and β-Sn phase, the characteristic peaks of dealloyed product belonged to Ag_3Sn intermetallic.

Further examination under TEM show that Ag_4Sn intermetallic certainly had dendrites composed of nanoparticles (Fig. 4a). On the surface of Ag_4Sn intermetallic (Fig. 4b), the distances between two neighboring crystal lattice fringes were 0.256 and 0.237 nm, which corresponded to the interplanar spacing of Ag_4Sn (100) and (002) planes. Ag_4Sn catalyst displays the typical polycrystalline structure with diffraction rings of (002), (101), (102), (110) and (200) facets that belong to the tetragonal phase, as shown from the selected-area electron diffraction (SAED) pattern in Fig. S6a. Ag_3Sn (Fig. 4c) shows

near-spherical particles with an average size of about 30 nm, the surface shows clear lattice fringes (0.238 and 0.260 nm) in Fig. 4d, which were assigned to the (002) and (110) planes of the orthorhombic Ag_3Sn phase. The SAED pattern in Fig. S6b shows five intense diffraction rings indexed to (110), (111), (112), (113) and (200) planes.

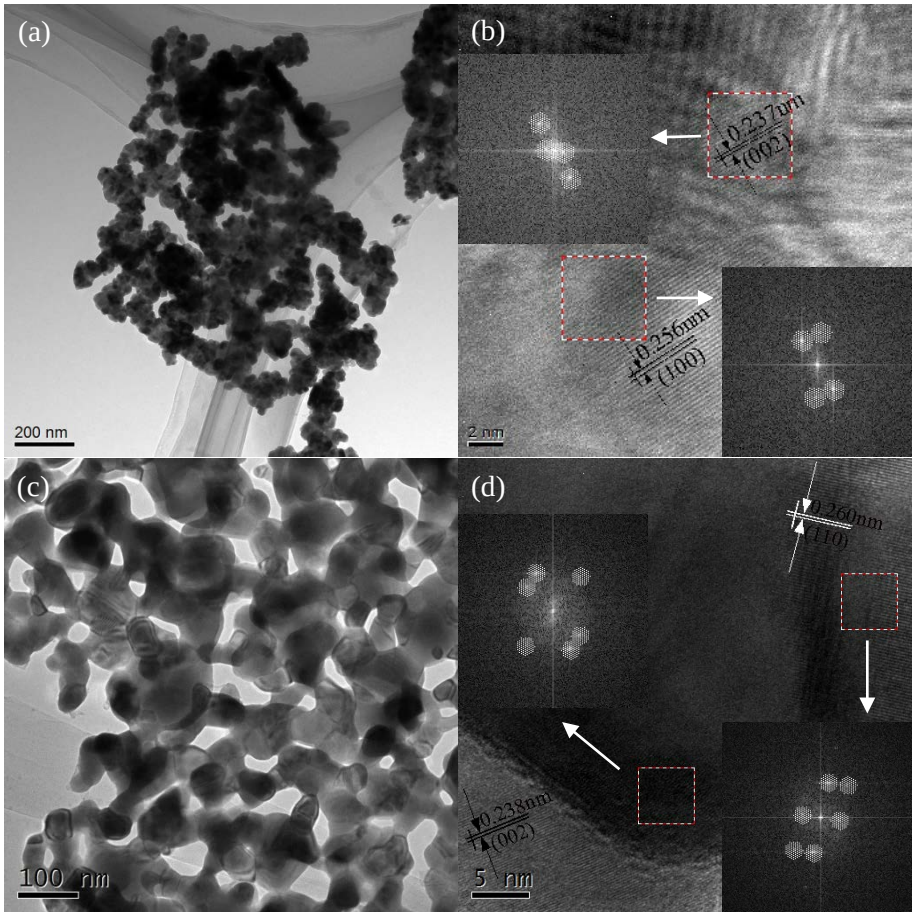

Fig. 4. (a, c) Bright field TEM images of the Ag_4Sn and Ag_3Sn catalysts. (b, d) HRTEM images of the Ag_4Sn and Ag_3Sn catalysts. The insets are the Fast Fourier Transform (FFT) patterns corresponding to the marked squares.

3.3. Selectivity of AgSn intermetallic catalysts toward the ORR

To study the effect of alcohol crossover on the cathodic oxygen reduction, the alcohol tolerance of the dealloying derived AgSn intermetallic catalysts was evaluated by adding

four alcohol concentrations (3 mM, 30 mM, 300 mM, 1 M) to the electrolyte. The LSV and CV curves in the presence of alcohols are obtained (Fig. 5 and Fig. S7). It is known to all that negative current values account for the ORR, while positive currents account for the alcohol oxidation reaction. As observed, the half-wave potentials for the Ag_4Sn and Ag_3Sn have almost no degradation and little loss of the current density in the presence of methanol or ethanol (Fig. 5(a,c) and Fig. S7(a,b)). Particularly, the ORR properties are little affected even at a high concentration of methanol up to 1.0 M. Moreover, the Ag_4Sn shows superior tolerance to ethanol and worse tolerance to methanol with respect to the Ag_3Sn. While, the ORR activity for the commercial Pt/C catalyst is significantly reduced in the present of alcohols even at a rather low concentration of 30 mM. The result is mainly caused by the competition between AOR and ORR on the Pt surface, resulting in the decline of the ORR current.

Furthermore, Fig. 5(e,f) compares CV curves of Ag_4Sn, Pt/C and PtRu/C catalysts in N_2-saturated 0.1 M KOH solution with and without the presence of 1.0 M alcohol. In alkaline media, the curves of the commercial Pt/C and PtRu/C catalysts do not exhibit alcohol oxidation features. After adding alcohol, there is an obvious alcohol oxidation peak in positive scan direction. Moreover, the comparison in current densities indicated that the PtRu/C showed higher catalytic activity for the AOR than that of the Pt/C. Nevertheless, the oxidation current is not observed in the CV curves of Ag_4Sn and Ag_3Sn. Further, the peaks related to oxide formation and reduction is depressed, especially with ethanol, which indicates that the alcohol is adsorbed on the surfaces without oxidation. Thus, the Ag_4Sn and Ag_3Sn catalysts demonstrate superior alcohol tolerance, which makes them proper for the DAFCs. As observed in Fig. 5(g,h), there is a little change in

the ORR current on Ag_4Sn after the addition of methanol or ethanol into the electrolyte solution, suggesting that alcohol does not affect original ORR catalytic activity of Ag_4Sn. While, once adding methanol or ethanol, the cathodic current measured on the commercial Pt/C and PtRu/C catalysts can shift to an anodic current, which confirms the

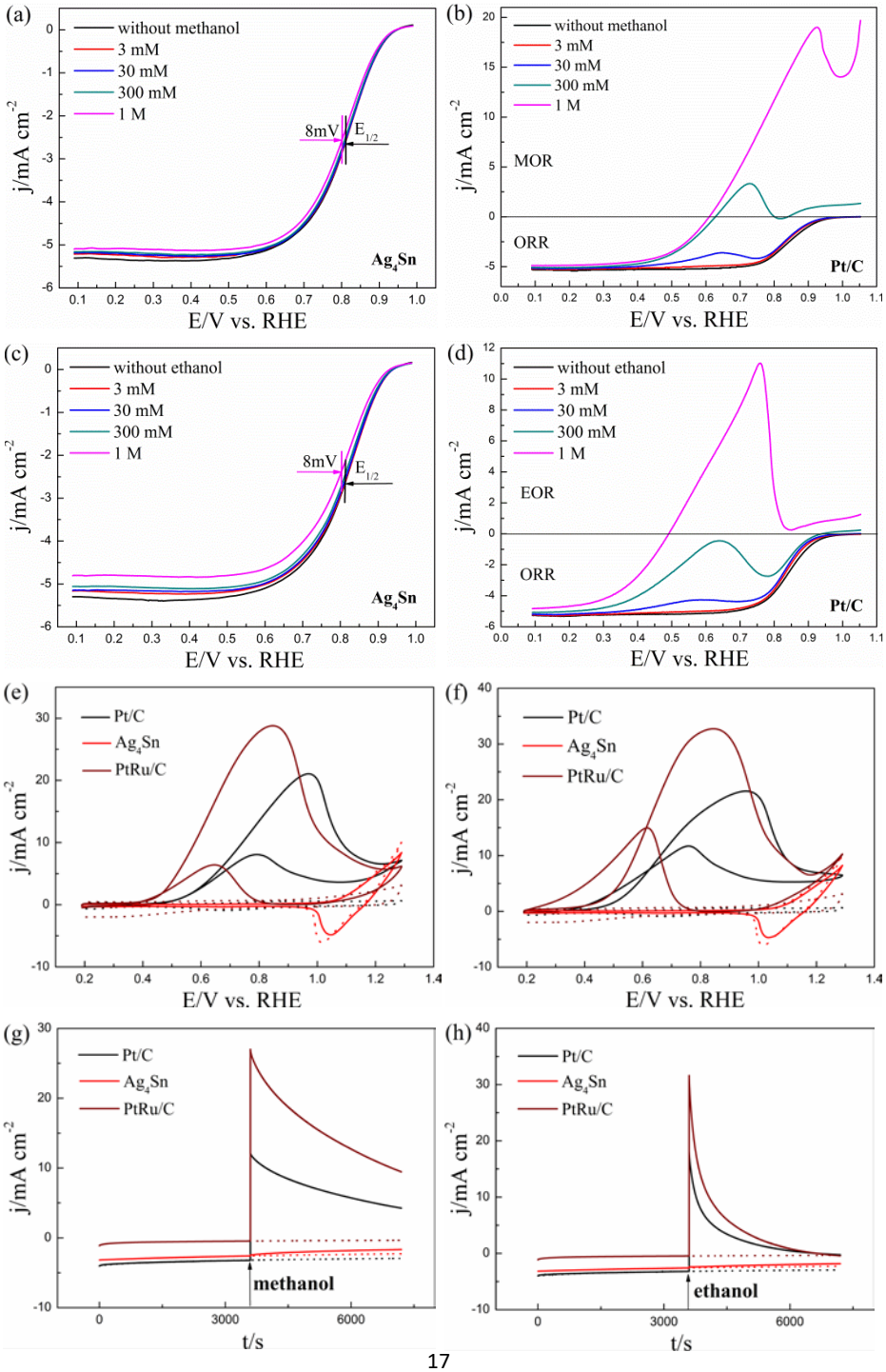

Fig. 5. (a-d) Effect of methanol or ethanol concentrations on the ORR for Ag_4Sn and Pt/C electrocatalysts in O_2-saturated 0.1 M KOH. Rotating rate: 1600 rpm; Sweep rate: 10 mV s^{-1}. (e, f) CV curves for Ag_4Sn, Pt/C, and PtRu/C catalysts in N_2-saturated 0.1 M KOH at a sweep rate of 50 mV s^{-1} in the presence of 1.0 M methanol or ethanol. The dot lines show the CVs for Ag_4Sn, Pt/C, and PtRu/C catalysts in N_2-saturated 0.1 M KOH. (g, h) Chronoamperometric responses of Ag_4Sn, Pt/C, and PtRu/C catalysts with alcohols added in O_2-saturated 0.1 M KOH. The dot lines show the chronoamperometric curves in alkaline solution without alcohols throughout the test.

AOR may compete with ORR in the presence of alcohols.

3.4. Durability of the Ag_4Sn intermetallic catalyst

In addition to the ORR activity and selectivity, the durability is also a significant determinant for the commercialization of fuel cells. To evaluate the stability of the dealloying derived Ag_4Sn intermetallic catalyst, the accelerated durability test (ADT) was

employed by continuously potential cycling between 0.6 and 1.1 V in O_2-saturated 0.1 M KOH solution at a scan rate of 50 mV s^{-1}. The peak current for Ag_4Sn was slightly decreased after 5000 potential cycles, as displayed in the inset of Fig. 6a. Pt/C exhibited a dramatical decay in the current for the peaks associated with the hydrogen adsorption/desorption under the same condition (the inset of Fig. 6c). Upon integration the charges, the ECSA on Ag_4Sn was decreased by only 24.8%, while 38.1% loss of

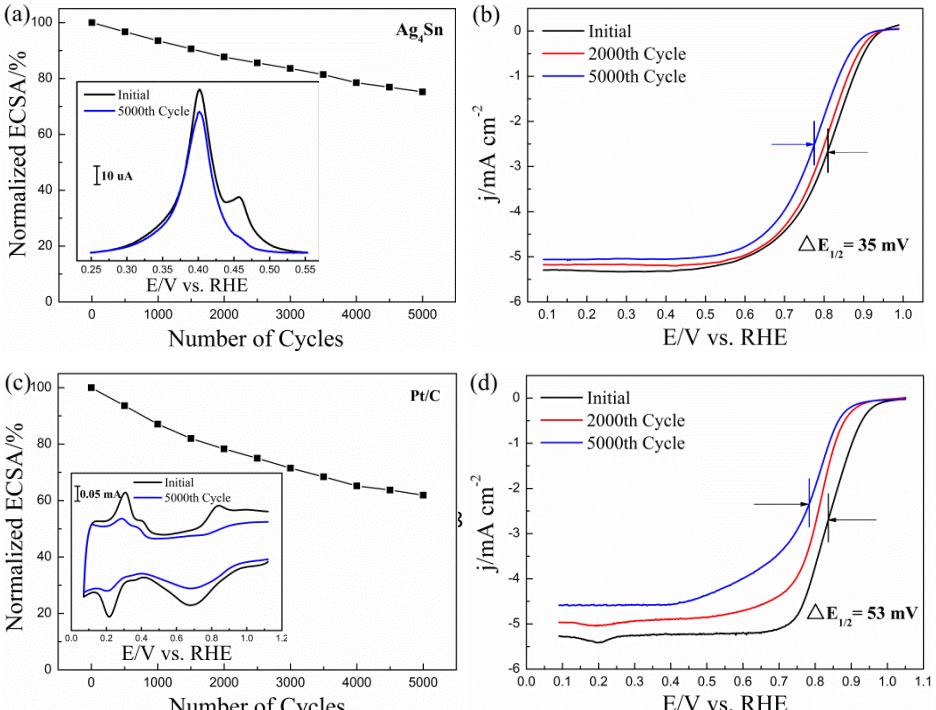

Fig. 6. (a, c) ECSA loss of the Ag_4Sn and Pt/C electrocatalysts with the number of cycles. Insets indicate the Pb-stripping voltammograms of Ag_4Sn electrocatalyst and CVs for Pt/C catalyst before and after 5000 cycles. (b, d) ORR polarization curves of the Ag_4Sn electrocatalyst and Pt/C catalyst after different number of cycles.

surface area on Pt/C was observed. Moreover, ORR polarization curves were also measured during the durability test. After 2000 cycles, the half-wave potential $E_{1/2}$ for Ag_4Sn decreased by 12 mV (Fig. 6b), while there is a 35-mV degradation in the corresponding $E_{1/2}$ for Pt/C (Fig. 6d). Even prolonging cycles to 5000, the $E_{1/2}$ in the Ag_4Sn exhibited a negative shift of 35 mV while in Pt/C it is almost 53 mV. As compared

in Figure 6, Ag_4Sn catalyst shows loss of 50.89% in specific activity at +0.85 V after 5000 cycles, while Pt/C catalyst shows 64.93% specific activity loss under the same condition. The ADT results indicate that Ag_4Sn intermetallic catalyst has extraordinarily superior stability to the Pt/C commercial catalyst. The dendritic and chemical ordered structure of Ag_4Sn intermetallic may be beneficial to the durability enhancement.

3.5. Origin of the superior catalytic activity of AgSn intermetallic catalysts

The enhanced activity towards ORR may be relevant to the surface species of catalysts [34], so the surface composition and electronic structure of the AgSn precursor alloys and dealloying derived intermetallic catalysts were analyzed by XPS (Fig. 7). The surface atomic ratios of Ag/Sn/O in different catalysts are compared in Table S1. As observed, the Ag:Sn:O atomic ratio on the surface of $Ag_{75}Sn_{25}$ is 55.13:18.47:26.40. Further increasing the deposition current to 25.5 mA cm^{-2}, the amount of Sn and O on the surface

increased. After dealloying, the content of Sn and O in Ag_4Sn and Ag_3Sn decreased. As shown in Fig. 7a, the Ag 3d peaks in different catalysts were split into Ag $3d_{3/2}$ and Ag $3d_{5/2}$ peaks, which can be ascribed to metallic Ag (0). The XPS peaks of Sn consisted of Sn $3d_{3/2}$ peak and Sn $3d_{5/2}$ peak, both of which were divided into metallic Sn and oxidized Sn peaks (Fig. 7b). The metallic Sn peaks centered at 484.8 and 493.2 eV. The calculated Sn (0) percentage in $Ag_{75}Sn_{25}$, Ag_4Sn, $Ag_{50}Sn_{50}$, and Ag_3Sn were 38.01, 42.71, 38.36, 53.87, respectively (Table S2), suggesting that Sn atoms oxide partially on the surface of the catalysts. The XPS spectra of O 1s revealed the contribution from both adsorbed oxygen (at 531.3 eV) and O^{2-} at the intrinsic sites (at 530.1 eV) (Fig. 7c).

Adzic et al. [37] reported that the difference in ORR activity in alkaline media is associated with the d-band center of the metal. In other words, metals with low d-band centers (e. g. Ag, Au) tend to possess low ORR activity because of the weak adsorption strength of oxygen. Metals with high d-band centers (e. g. Ir, Pd) also have poor ORR activity, owing to the difficult desorption of the oxygenated intermediates, even when the O-O bonds split easily. Nørskov et al. [38] reported that the relative position of the d-band center can be used as a simple descriptor for ORR activity. To investigate the catalytic mechanism of ORR on Ag_4Sn and Ag_3Sn catalysts, the valence band spectrum (VBS) of the AgSn precursor alloys and dealloying derived intermetallic catalysts was also measured, as shown in Fig. 7d, the d-band centers of $Ag_{75}Sn_{25}$, Ag_4Sn, $Ag_{50}Sn_{50}$, and Ag_3Sn were at -5.42, -5.37, -5.51, and -5.40 eV, respectively. Moreover, β-Sn phase in $Ag_{75}Sn_{25}$ and $Ag_{50}Sn_{50}$ precursor alloy lead to the downshift of the d-band center of the nanoparticles. It is unexpected that the d-band centers of Ag_4Sn and Ag_3Sn catalysts are more far away from the Fermi level relative to pure Ag with the d-band center at -

5.34 eV. This is distinctly different from that on Ag-based alloys, where the rise in d-band center results in stronger adsorption to oxygen, thereby improving ORR activity [39].

The Ag_4Sn catalyst had a lower d-band center but better ORR activity compared to pure Ag, which makes it difficult to rationalize the enhanced activity simply by the d-band shifting. The surface species of Ag_4Sn catalyst are composed of Ag, Sn, and SnO_x, as confirmed by XPS analysis. Sn is known to have stronger oxygen binding than Ag, which is the rate-determined step of the ORR process. Nevertheless, the enhanced absorption of oxygen is at the expense of forming strongly bound OH^-, which inhibits the release of OH^-. Moreover, the experimental VBS results have inferred that OH^- binds more weakly to Ag_4Sn than to Ag. Due to the weak interaction between OH^- and the Ag_4Sn catalyst, the surfaces of the catalyst have lower coverage of OH^-, which promotes the final step of ORR process. Therefore, it is most likely that the ensemble effect exists to make use of the capability of Sn for initial O_2 binding and the capability of Ag for fast removal of the oxygenated intermediates. In addition, fish-like dendrites have larger accessible surface area and more exposed catalytic active sites, which are good for boosting the ORR activity.

Working on ensemble effect, the Ag_4Sn catalyst consists of two different metals catalyzing the distinct steps in the ORR process. As displayed in Fig. 7e, O_2 is chemisorbed onto Sn and Sn oxide sites in the form of $(O_2^{\bullet-})_{ads}$, the $(O_2^{\bullet-})_{ads}$ then spill over onto the Ag sites and subsequently is reduced on Ag sites. The hydroxyl species (OH^-) could easily leave the surface, which could then generate free active sites for further reduction. In this way, the full four-electron process can be achieved by

combining the fast kinetics of Sn for the first one-electron reduction (eq 2) with reduction of $(O_2^{\bullet -})_{ads}$ on Ag (eq3-6) and the rapid disproportionation ($2HO_2^- \rightarrow 2OH^- + O_2$). So the ORR pathway on the Ag_4Sn catalyst proceeds via a five-step surface-mediated mechanism [40-42]:

$$O_2 + e^- \rightarrow (O_2^{\bullet -})_{ads} \quad (2)$$

$$(O_2^{\bullet -})_{ads} + H_2O \rightarrow (HO_2^{\bullet})_{ads} + OH^- \quad (3)$$

$$(HO_2^{\bullet})_{ads} + e^- \rightarrow HO_2^- \quad (4)$$

$$O_{ads} + H_2O + e^- \rightarrow OH_{ads} + OH^- \quad (5)$$

$$OH_{ads} + e^- \rightarrow OH^- \quad (6)$$

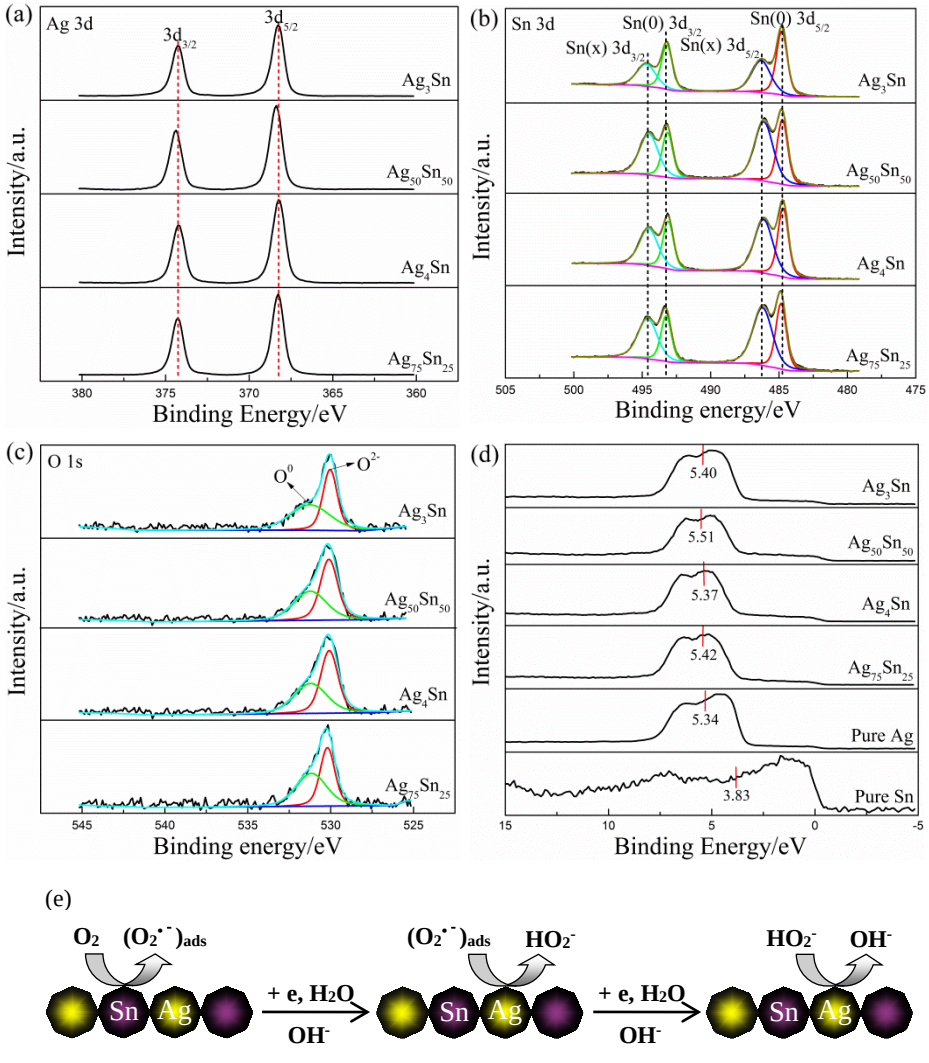

Fig. 7. (a-c) The high-resolution XPS spectra of the Ag 3d, Sn 3d, and O 1s for AgSn precursor alloy and dealloying derived catalysts. (d) Valence band spectrum (VBS) for AgSn precursor alloy and dealloying derived catalysts. The red vertical bars represent the d-band center positions. This shows that the d-band centers of the Ag_4Sn and Ag_3Sn catalysts shift away from the Fermi level compared to pure Ag. (e) Schematic diagram of the catalytic mechanism of the Ag_4Sn and Ag_3Sn catalysts where oxygen adsorbs on the Sn as $(O_2^{\bullet-})_{ads}$ and $(O_2^{\bullet-})_{ads}$ is subsequently reduced to OH^- on the Ag.

3.6. Performance of the membraneless alkaline fuel cell

A schematic for the membraneless alkaline Zn-air battery and DAFC is illustrated in Fig. 8a. The performance of the membraneless alkaline fuel cell is mainly limited by the dissolved oxygen [43], so we designed the air electrode for utilizing oxygen in the air. The membraneless alkaline Zn-air battery was first studied, in which a zinc plate was used as the anode fuel and AgSn intermetallics as the cathode catalysts. The discharge polarization curves and power density curves are presented in Fig. 8b. For comparison, the Pt/C-based battery had an open-circuit voltage (OCV) of 1.50 V and a power density of 94.09 mW cm^{-2} at a discharge current density of 100 mA cm^{-2}. The OCVs for Ag_4Sn and Ag_3Sn were measured to be 1.41 V and 1.36 V, respectively. At a high discharge current density, the maximum power densities for Ag_4Sn and Ag_3Sn were calculated as 80.12 and 77.44 mW cm^{-2}. Clearly, the Ag_4Sn displayed superior discharge performance. The galvanostatic charge-discharge behavior of rechargeable Zn-air batteries were investigated in Fig. 8c and Fig. S8a, in which AgSn intermetallics demonstrated very stable charge-discharge cyclic performance compared to commercial Pt/C.

In the membraneless alkaline DAFC, an aqueous solution consists of alcohol as the anode fuel and KOH as the supporting electrolyte. Commercial Pt/C and PtRu/C were employed as anode catalysts, and AgSn intermetallics were employed as cathode

catalysts. The AgSn intermetallics at the cathode efficiently catalyze O_2 reduction without oxidizing the alcohol. Unlike AgSn intermetallics, the Pt/C at the anode catalyzes both AOR and ORR. LSV curves shown in Fig. 5 reveal that at a high alcohol concentration (more than 300 mM), alcohol oxidation dominates the current response at the Pt/C relative to the ORR, thus, the crossover of O_2 is not a significant problem in this prototype when the O_2 concentration in the air is far lower than the concentration of the alcohol (as high as 5 M). As manifested by Fig. 5(e,f) and Fig. S2, PtRu/C displayed superior catalytic activity towards the AOR but poor ORR activity than that of the Pt/C, which renders it a good candidate as a selective catalyst for AOR at anode of DAFC. Furthermore, the supporting electrolyte KOH sustains the migration of OH^-. Therefore, it seems to be feasible to omit the anion-exchange membrane used in the traditional alkaline DAFCs.

As shown in Fig. S8(b,c), with either Pt/C or PtRu/C as the anode catalyst, if the membraneless alkaline DMFC was measured with commercial Pt/C cathode catalyst, undesirable AOR at the cathode could occur, thereby poisoning Pt catalyst and decreasing the OCV to 0.1 V. In contrast, the membraneless alkaline DMFCs operating with Ag_4Sn and Ag_3Sn cathode catalysts maintained the stable OCVs of above 0.49 V for 1 h. More importantly, the membraneless alkaline DMFC using the PtRu/C at the anode displayed higher OCV than the same membraneless fuel cell using the Pt/C at the anode. The polarization curves and power density plots of the membraneless alkaline DMFCs and DEFCs are presented in Fig. 8(d-g). It is noteworthy to mention that the membraneless alkaline DMFCs and DEFCs using either Ag_4Sn or Ag_3Sn as cathode catalyst and Pt/C as anode catalyst delivered OCVs of about 0.7 V. The membraneless

alkaline DMFC with Ag_3Sn cathode catalyst had a maximum power density of 3.0 mW cm^{-2}; however, for the Ag_4Sn cathode catalyst, the value was 2.26 mW cm^{-2}. Ag_4Sn-based alkaline DEFC displayed a peak power density of 1.38 mW cm^{-2}, while Ag_3Sn-based DEFC only achieved a peak power density of 1.27 mW cm^{-2}. In case of PtRu/C catalysts, the performance of the membraneless alkaline DMFC and DEFC is improved significantly. The DMFCs with Ag_4Sn and Ag_3Sn cathode catalysts had the maximum power density of 4.46 mW cm^{-2} and 5.59 mW cm^{-2}, respectively. However, the

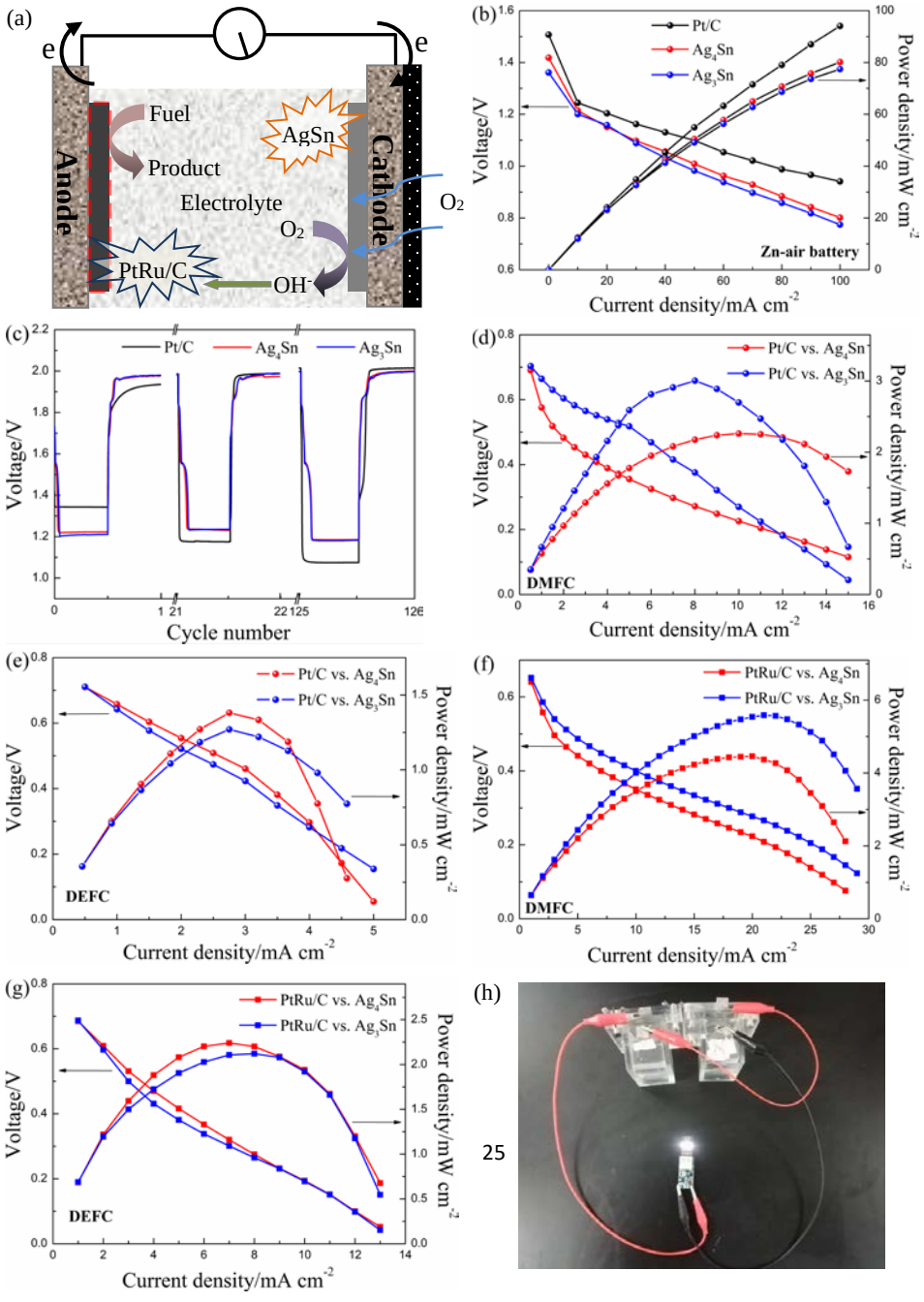

Fig. 8. (a) Schematic for the membraneless alkaline Zn-air battery and DAFC composed of a single chamber with the fuel electrode and the air electrode in KOH electrolyte. The fuel at the anode in Zn-air battery and DAFC is zinc and alcohol, DAFC requires the use of Pt/C (denoted with the dotted box) to catalyze alcohol oxidation. (b) The discharge polarization curves and power density curves for the membraneless alkaline Zn-air batteries. (c) Galvanostatic charge-discharge cycling curves of rechargeable Zn-air batteries at a current density of 5 mA cm^{-2} for 125 cycles with 2 h charge-2 h discharge period. (d-g) The polarization curves and power density plots of the membraneless alkaline DAFCs using Pt/C (or PtRu/C) as the anode catalyst and AgSn intermetallics as cathode catalysts. (h) Digital photograph of a LED lamp powered by two membraneless alkaline DMFCs with Ag_3Sn cathode catalyst connected in series.

maximum power density of the DEFCs was 2.24 and 2.12 mW cm^{-2} for Ag_4Sn and Ag_3Sn, respectively. It clearly indicates that the performance trends are consistent with the higher AOR activity and better tolerance to alcohol in Fig. 5 and Fig. S7. Two membraneless alkaline DMFC were connected in series and used to light a LED lamp, as shown in Fig. 8h, suggesting the potential practical utilization of the membraneless alkaline DMFC.

In a recent study, Yang et al. [44] have reported an OCV of 0.38 V and a maximum power of 15 μW employing the Au@Ag_2S@Pt nanocomposites at the anode and the Pt-Ru nanoparticles at the cathode in the membraneless DMFC. The membrane-free DMFC built up with the CuO/N-rGO cathode and Pt/C anode gave an OCV of 0.5 V and a peak power density of 0.61 mW cm^{-2} [45]. Osaka et al. [46] proposed a micro DMFC of an air-breathing, membraneless, and monolithic design using a Pt-Ru alloy for the anode and a Pd-Co alloy for the cathode. The maximum power was 1.4 μW, and the OCV was 0.50 V. It is clear that the present membraneless alkaline DMFCs with the AgSn intermetallics cathode and the PtRu/C anode demonstrate a higher OCV and maximum power density than the state-of-the-art works. Although the performance of the prototype cell is lower

than the membrane based DMFC, we believe that developing a good oxygen tolerant anode catalyst, modifying cell designs and optimizing the operating conditions (the concentration of the fuel, flow rate of anolytes, operating temperature) will result in further improvements in the performance.

4. Conclusions

In summary, we have shown rapid synthesis of ordered Ag_4Sn and Ag_3Sn intermetallics with different nanostructures. Based on XRD, SEM and TEM results, it is found that the intermetallic and β-Sn phases were initially formed, followed by the dissolution of Sn due to the potential cycling, and then the pure intermetallic phase was obtained. Electrocatalytic tests demonstrate that the Ag_4Sn intermetallic shows better activity towards ORR in terms of $E_{1/2}$, Tafel slope, ECSA, and SA in comparison with Ag_3Sn. Additionally, the Ag_4Sn presents superior tolerance to ethanol and worse tolerance to methanol with respect to the Ag_3Sn. Compared to Pt/C, the Ag_4Sn also shows improved durability after 5000 potential cycles. The increase in catalytic activity is mainly ascribed to the ensemble effect and strong chemical bond in the ordered intermetallic structure. Using AgSn intermetallics as the cathode catalysts, the membraneless alkaline zinc-air battery and DAFC is able to deliver a high power density. This work would be further extended to the future design and construction of bimetallic alloy with high performance and excellent tolerance to alcohol for the alkaline fuel cells.

Conflicts of interest

All the authors declare that they have no conflict of interest.

Acknowledgements

This work was supported by the National Natural Science Foundation of China (grant no. 51874243, 51271148 and 50971100), the Research Fund of State Key Laboratory of Solidification Processing in China (grant no. 150-ZH-2016), the Aeronautic Science Foundation Program of China (grant no. 2012ZF53073), the Project of Transformation of Scientific and Technological Achievements of NWPU (grant no. 19-2017), the Doctoral Fund of Ministry of Education of China (grant no. 20136102110013), and the Open Fund of State Key Laboratory of Advanced Technology for Materials Synthesis and Processing (Wuhan University of Technology grant no. 2018-KF-18). We would like to thank the Analytical & Testing Center of Northwestern Polytechnical University for SEM and TEM characterizations.

Appendix A. Supplementary data

The following is Supplementary data to this article:

References

[1] T.S. Zhou, Y. Zhou, R.G. Ma, Z.Z. Zhou, G.H. Liu, Q. Liu, Y.F. Zhu, J.C. Wang, Nitrogen-doped hollow mesoporous carbon spheres as a highly active and stable metal-free electrocatalyst for oxygen reduction, Carbon 114 (2017) 177-186.

[2] G.Q. Zhang, B.Y. Xia, X. Wang, X.W. (David) Lou, Strongly coupled $NiCo_2O_4$-rGO hybrid nanosheets as a methanol-tolerant electrocatalyst for the oxygen reduction reaction, Adv. Mater. 26 (2014) 2408-2412.

[3] N. Benipal, J. Qi, Q. Liu, W.Z. Li, Carbon nanotube supported PdAg nanoparticles for electrocatalytic oxidation of glycerol in anion exchange membrane fuel cells, Appl. Catal. B Environ. 210 (2017) 121-130.

[4] X. Wei, D. Desai, G.G. Yadav, D.E. Turney, A. Couzis, S. Banerjee, Impact of anode substrates on electrodeposited zinc over cycling in zinc-anode rechargeable alkaline batteries, Electrochim. Acta 212 (2016) 603-613.

[5] D. Desai, X. Wei, D.A. Steingart, S. Banerjee, Electrodeposition of preferentially oriented zinc for flow-assisted alkaline batteries, J. Power Sources 256 (2014) 145-152.

[6] Y.S. Li, Y. Feng, X.D. Sun, Y.L. He, A sodium-ion-conducting direct formate fuel cell: generating electricity and producing base, Angew. Chem. Int. Ed. 56 (2017) 5734-5737.

[7] X.W. Yu, A. Manthiram, Catalyst-selective, scalable membraneless alkaline direct formate fuel cells, Appl. Catal. B Environ. 165 (2015) 63-67.

[8] R. Zeng, J. Handsel, S.D. Poynton, A.J. Roberts, R.C.T. Slade, H. Herman, D.C. Apperley, J.R. Varcoe, Alkaline ionomer with tuneable water uptakes for electrochemical energy technologies, Energ. Environ. Sci. 4 (2011) 4925-4928.

[9] B. Yan, N.M. Concannon, J.D. Milshtein, F.R. Brushett, Y. Surendranath, A membrane-free neutral pH formate fuel cell enabled by a selective nickel sulfide oxygen reduction catalyst, Angew. Chem. Int. Ed. 56 (2017) 1-5.

[10] D.D. James, P.G. Pickup, Effects of crossover on product yields measured for direct ethanol fuel cells, Electrochim. Acta 55 (2010) 3824-3829.

[11] M.A. Goulet, E. Kjeang, Co-laminar flow cells for electrochemical energy conversion, J. Power Sources 260 (2014) 186-196.

[12] K.S. Salloum, J.D. Posner, A membraneless microfluidic fuel cell stack, J. Power Sources 196 (2011) 1229-1234.

[13] M.R. Thorson, F.R. Brushett, C.J. Timberg, P.J.A. Kenis, Design rules for electrode arrangement in an air-breathing alkaline direct methanol laminar flow fuel cell, J. Power Sources 218 (2012) 28-33.

[14] X.W. Yu, E.J. Pascual, J.C. Wauson, A. Manthiram, A membraneless alkaline direct liquid fuel cell (DLFC) platform developed with a catalyst-selective strategy, J. Power Sources 331 (2016) 340-347.

[15] L. Osmieria, R. Escudero-Cidb, M. Armandia, A.H.A.M. Videlaa, J.L.G. Fierroc, P. Ocónb, S. Specchia, Fe-N/C catalysts for oxygen reduction reaction supported on

different carbonaceous materials. Performance in acidic and alkaline directalcohol fuel cells, Appl. Catal. B Environ. 205 (2017) 637-653.

[16] Y.Q. Hua, T.T. Jiang, K. Wang, M.M. Wu, S.Q. Song, Y. Wang, P. Tsiakaras, Efficient Pt-free electrocatalyst for oxygen reduction reaction: Highly ordered mesoporous N and S co-doped carbon with saccharin as single-source molecular precursor, Appl. Catal. B Environ. 194 (2016) 202-208.

[17] H.Y. Park, J.H. Park, P. Kim, S.J. Yoo, Hollow $PdCu_2$@Pt core@shell nanoparticles with ordered intermetallic cores as efficient and durable oxygen reduction reaction electrocatalysts, Appl. Catal. B Environ. 225 (2017) 84-90.

[18] J.H. Yang, W.J. Zhou, C.H. Cheng, J.Y. Lee, Z.L. Liu, Pt-decorated PdFe nanoparticles as methanol-tolerant oxygen reduction electrocatalyst, ACS Appl. Mater. Interfaces 2 (2010) 119-126.

[19] N. Zhang, Y.G. Feng, X. Zhu, S.J. Guo, J. Guo, X.Q. Huang, Superior bifunctional liquid fuel oxidation and oxygen reduction electrocatalysis enabled by PtNiPd core-shell nanowires, Adv. Mater. (2017) 1603774-1603780.

[20] G.T. Fu, K. Wu, J. Lin, Y.W. Tang, Y. Chen, Y.M. Zhou, T.H. Lu, One-pot water-based synthesis Pt-Pd alloy nanoflowers and their superior electrocatalytic activity for the oxygen reduction reaction and remarkable methanol-tolerant ability in acid media, J. Phys. Chem. C 117 (2013) 9826-9834.

[21] G.T. Fu, X. Jiang, M.X. Gong, Y. Chen, Y.W. Tang, J. Lin, T.H. Lu, Highly branched platinum nanolance assemblies by polyallylamine functionalization as superior active, stable, and alcohol-tolerant oxygen reduction electrocatalysts, Nanoscale 6 (2014) 8226-8234.

[22] D.T. Zhang, F.X. Wu, M.H. Peng, X.Y. Wang, D.G. Xia, G.S. Guo, One-Step, Facile and ultrafast synthesis of phase- and size- controlled Pt-Bi intermetallic nanocatalysts through continuous-flow microfluidics, J. Am. Chem. Soc. 137 (2015) 6263-6269.

[23] P. Anandha Ganesh, D. Jeyakumar, One pot aqueous synthesis of nanoporous $Au_{85}Pt_{15}$ material with surface bound Pt islands: an efficient methanol tolerant ORR catalyst, Nanoscale 6 (2014) 13012-13021.

[24] Y.H. Cho, O.H. Kim, D.Y. Chung, H. Choe, Y.H. Cho, Y.E. Sung, PtPdCo ternary electrocatalyst for methanol tolerant oxygenreduction reaction in direct methanol fuel cell, Appl. Catal. B Environ. 154-155 (2014) 309-315.

[25] J.N. Zheng, L.L. He, F.Y. Chen, A.J. Wang, M.W. Xue, J.J. Feng, Simple one-pot synthesis of platinum-palladium nanoflowers withenhanced catalytic activity and methanol-tolerance for oxygenreduction in acid media, Electrochim. Acta 137 (2014) 431-438.

[26] L.L. Zou, J. Fan, Y. Zhou, C.M. Wang, J. Li, Z.Q. Zou, H. Yang, Conversion of PtNi alloy from disordered to ordered for enhanced activity and durability in methanol-tolerant oxygen reduction reactions, Nano Res. 8 (2015) 2777-2788.

[27] M.R. Gao, Q. Gao, J. Jiang, C.H. Cui, W.T. Yao, S.H. Yu, A methanol-tolerant Pt/$CoSe_2$ nanobelt cathode catalyst for direct methanol fuel cells, Angew. Chem. 123 (2011) 5007-5010.

[28] L.M. Shen, T. Sun, O. Zhuo, R.C. Che, D.Q. Li, Y.C. Ji, Y.F. Bu, Q. Wu, L.J. Yang, Q. Chen, X.Z. Wang, Z. Hu, Alcohol-tolerant platinum electrocatalyst for oxygen reduction by encapsulating platinum nanoparticles inside nitrogen-doped carbon nanocages, ACS Appl. Mater. Interfaces 8 (2016) 16664-16669.

[29] J.K. Nørskov, J. Rossmeisl, A. Logadottir, L. Lindqvist, Origin of the overpotential for oxygen reduction at a fuel-cell cathode, J. Phys. Chem. B 108 (2004) 17886-17892.

[30] N. Zhang, F.Y. Chen, X.Q. Wu, Q. Wang, A. Qaseem, Z. H. Xia, Activity origin of core-shell and alloy AgCu bimetallic nanoparticles for oxygen reduction reaction, J. Mater. Chem. A 5 (2017) 7043-7054.

[31] R.C. Sekol, X.K. Li, P. Cohen, G. Doubek, M. Carmo, A.D. Taylor, Silver palladium core-shell electrocatalyst supported on MWNTs for ORR in alkaline media, Appl. Catal. B Environ. 138-139 (2013) 285-293.

[32] L. Zeng, T.S. Zhao, L. An, A high-performance supportless silver nanowire catalyst for anion exchange membrane fuel cells, J. Mater. Chem. A 3 (2015) 1410-1416.

[33] K. Ni, L. Chen, G.X. Lu, Synthesis of silver nanowires with different aspect ratios as alcohol-tolerant catalysts for oxygen electroreduction, Electrochem. Commun. 10 (2008) 1027-1030.

[34] Y.J. Lu, N.L. Zhang, L. An, X. Li, D.G. Xia, Synthesis of high dispersed intermetallic Ag_4Sn/C and its enhanced oxygen reduction reaction activity, J. Power Sources 240 (2013) 606-611.

[35] Q. Wang, F.Y. Chen, Y.X. Liu, N. Zhang, L. An, R.L. Johnston, Bifunctional electrocatalysts for oxygen reduction and borohydride oxidation reactions using Ag_3Sn nano-intermetallic on ensemble effect, ACS Appl. Mater. Interfaces 9 (2017) 35701-35711.

[36] Y.X. Liu, F.Y. Chen, Q. Wang, J.P. Wang, J.L. Wang, Direct unassisted hydrogen peroxide generation from oxygen and water on plasmonic Ag-graphene-Cu nanosandwitch, Appl. Catal. B Environ. 224 (2018) 940-950.

[37] F.H.B. Lima, J. Zhang, M.H. Shao, K. Sasaki, M.B. Vukmirovic, E.A. Ticianelli, R.R. Adzic, Catalytic activity-d-band center correlation for the O_2 reduction reaction on platinum in alkaline solutions, J. Phys. Chem. C 111 (2007) 404-410.

[38] T. Bligaard, J.K. Nørskov, Ligand effects in heterogeneous catalysis and electrochemistry, Electrochim. Acta 52 (2007) 5512-5516.

[39] X.Q. Wu, F.Y. Chen, N. Zhang, Y.M. Lei, Y.C. Jin, A. Qaseem, R.L. Johnston, Activity trends of binary silver alloy nanocatalysts for oxygen reduction reaction in alkaline Media, Small (2017) 1603387.

[40] D.A. Slanac, W.G. Hardin, K.P. Johnston, K.J. Stevenson, Atomic ensemble and electronic effects in Ag-rich AgPd nanoalloy catalysts for oxygen reduction in alkaline media, J. Am. Chem. Soc. 134 (2012) 9812-9819.

[41] L. Yu, X.L. Pan, X.M. Cao, P. Hu, X.H. Bao, Oxygen reduction reaction mechanism on nitrogen-doped graphene: A density functional theory study, J. Catalysis 282 (2011) 183-190.

[42] S.Z. Liu, M.G. White, P. Liu, Mechanism of oxygen reduction reaction on Pt(111) in alkaline solution: importance of chemisorbed water on surface, J. Phys. Chem. C 120 (2016) 15288-15298.

[43] S. Tominaka, S. Ohta, T. Osaka, R. Alkire, Prospects of on-chip fuel cell performance: Improvement based on numerical simulation, Energy Environ. Sci. 4 (2010) 162-171.

[44] Y. Feng, J.H. Yang, H. Liu, F. Ye, J. Yang, Selective electrocatalysts toward a prototype of the membraneless direct methanol fuel cell, Sci. Rep. 4 (2014) 3813.
[45] R.F. Zhou, Y. Zheng, D.H. Jurcakova, S.Z. Qiao, Enhanced electrochemical catalytic activity by copper oxide grown on nitrogen-doped reduced graphene oxide, J. Mater. Chem. A 1 (2013) 13179-13185.
[46] S. Tominaka, S. Ohta, H. Obata, T. Momma, T. Osaka, On-chip fuel cell: micro direct methanol fuel cell of an air-breathing, membraneless, and monolithic design, J. Am. Chem. Soc. 130 (2008) 10456-10457.